Journal of Physics:
Conference Series

PAPER • **OPEN ACCESS**

Aeroelastic Coupled Mode Behavior of Swept Composite Wing

To cite this article: E. Elshazly *et al* 2025 *J. Phys.: Conf. Ser.* **3070** 012001

Journal of Physics: Conference Series **3070** (2025) 012001 doi:10.1088/1742-6596/3070/1/012001

Aeroelastic Coupled Mode Behavior of Swept Composite Wing

E. Elshazly[1], Mohammed Kassem[1*] and M. A. Elshafei[1]

[1]Department of Aircraft Mechanics, Military Technical College, CAIRO, EGYPT

[*]E-mail: m_kassem@mtc.edu.eg

Abstract. The aeroelastic behavior of swept composite wings is predominantly governed by the coupling between bending and torsion modes due to the anisotropic characteristics of composite materials. This study analytically investigates the aeroelastic response of swept rectangular wings, modeled as carbon fiber/epoxy plates, to determine flutter and divergence speeds. The analytical approach integrates classical plate theory, Rayleigh-Ritz energy formulation, potential and kinetic energy equations, and unsteady incompressible two-dimensional aerodynamic theory within the Lagrange framework for free vibration and aeroelastic analyses. Numerical free vibration analysis is conducted using NASTRAN to validate the proposed analytical model. V-g curves are employed to extract flutter and divergence speeds, and the results exhibit excellent agreement with published findings. The study reveals that negative bending-torsion coupling stiffness significantly increases the likelihood of divergence occurring before flutter. Positive bending-torsion coupling significantly increases the divergence speed, effectively shifting the critical divergence speed beyond the typical flight envelope. Moreover, increasing the sweepback angle generally increases divergence speed. The effect on flutter speed is complex and depends on various factors, such as fiber orientation, stacking sequence, and bending-torsion coupling. These findings provide critical insights into aeroelastic behavior and offer a foundation for optimizing the performance and structural design of swept composite wings.

1. Introduction

The study of aeroelastic behavior in swept composite wings has garnered significant attention due to the complex interaction between structural dynamics and aerodynamic forces, particularly in applications involving high-performance aircraft. Several researchers have investigated various aspects of this behavior, focusing on the influence of bending-torsion stiffness coupling, sweep angle, and composite material properties.

Hollowell et al. [1] examined the influence of bending-torsion stiffness coupling on the aeroelastic behavior of wings, utilizing a Rayleigh-Ritz energy formulation in combination with unsteady, two-dimensional aerodynamic theory to predict flutter and divergence velocities. These predictions were validated against low-speed wind tunnel tests, which confirmed that positive bending-torsion coupling can effectively delay or eliminate divergence while also influencing stall flutter behavior. This coupling is essential in the design of swept wings, as it can enhance structural stability under aerodynamic loading.

Lottati et al. [2] also investigated the aeroelastic behavior of a cantilevered, composite, forward-swept rectangular wing, employing an analytical approach based on incompressible, two-dimensional unsteady aerodynamic strip theory. The study highlighted a critical trade-off between flutter velocity and divergence speed, showing that maximizing flutter velocity often leads to a decrease in divergence speed. This emphasizes the need to balance these competing factors in the design of composite wings to optimize their aeroelastic performance.

The impact of aspect ratio and sweep angle on aeroelastic behavior has also been explored. Attaran et al. [3] analyzed the flutter characteristics of composite wings, focusing on the effects of aspect ratio, sweep angle, and stacking sequence on flutter speed. Parametric studies revealed that forward-swept configurations exhibit higher flutter speeds but are constrained by divergence, which is influenced by

the structural properties of the composite materials and the stacking sequence. Similarly, Bach et al. [4] studied forward-swept composite wings, emphasizing the significance of bend-twist coupling, which mitigates aeroelastic divergence and enhances performance at varying sweep angles. Optimized stacking sequences were shown to reduce structural mass while maintaining aerodynamic efficiency.

Farsadi et al. [5] investigated the coupled mode behavior of swept composite wings, focusing on the influence of bending and torsion slopes, which affect the effective angle of attack and downwash velocity. The study found that the sweep angle plays a critical role, with increased sweep leading to higher response amplitudes and longer damping times, indicating a complex interaction between structural dynamics and aerodynamic forces. These findings highlight the importance of understanding the coupled dynamics in swept wings to improve aeroelastic performance.

In addition to the structural design considerations, Ibrahim et al. [6] explored the potential for suppressing wing flutter through parametric excitation, a technique known to stabilize certain dynamic systems. This approach, which induces excitation along the wing's plane of highest rigidity, was analyzed for its ability to stabilize the wing near the critical flutter speed. The use of nonlinear analysis and bifurcation diagrams further expanded the understanding of the conditions under which parametric excitation can suppress flutter.

Further studies have provided additional insights into the design of composite wings. Guo et al. [7] focused on forward-swept wings and highlighted the trade-off between maximizing flutter velocity and minimizing divergence speed, underscoring the importance of considering these factors in the design process. Fabbiane et al. [8] proposed a bi-objective optimization strategy to alleviate static and dynamic aeroelastic loads in composite wings, though without specific consideration of coupled mode behavior. Meanwhile, Ritter et al. [9] investigated forward-swept composite wings through unsteady test cases, emphasizing the importance of inertial coupling and highlighting the role of finite element models in capturing the first bending mode frequency.

Xue et al. [10] discussed the optimization of composite material properties and stacking sequences to enhance the aeroelastic performance of forward-swept wings, with an emphasis on torsion divergence and structural deformation. The study used surrogate models to analyze the relationship between design variables and structural deformation, offering a new perspective on optimizing wing performance under specific loading conditions. Similarly, Kawakami et al. [11] focused on the aeroelastic characteristics of aft-swept composite wings, using a minimum weight design approach to enhance structural damping while ensuring flutter and divergence speed constraints.

Finally, Farsadi et al. [12] and Kameyama et al. [13] presented multidisciplinary design optimization approaches for composite wings, integrating nonlinear aeroelastic analyses and structural damping to improve performance. Maharan et al. [14] employed finite element methods to analyze composite plate swept wings, incorporating advanced modeling techniques to enhance the accuracy of aeroelastic predictions for complex composite structures.

These studies collectively highlight the intricate behavior of swept composite wings under aeroelastic loading, with particular emphasis on the critical role of bending-torsion stiffness coupling, sweep angle, and material properties in determining the stability and performance of these wings. The findings from these investigations provide a comprehensive foundation for further exploration into the coupled mode behavior of swept composite wings, offering valuable insights for the design of more efficient and stable aeroelastic systems.

The current research discusses straight and swept wings and compares the proposed model's results with the published data. It uses an analytical approach and a finite element method to show the swept wing's effect on flutter and divergence speeds.

2. MATHEMATICAL MODELING

The coordinate system and the geometry of the laminated wing, with a sweep angle (Λ), chord length (c), span length (l), and plate thickness (t), are shown in Fig.1.

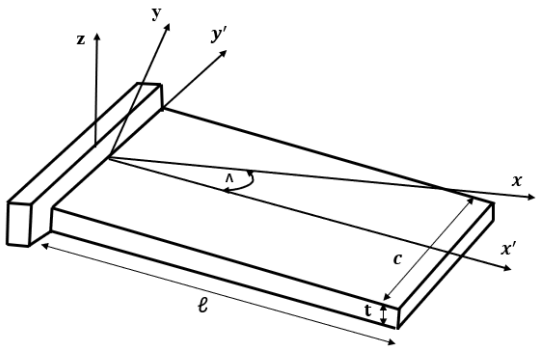

Figure 1 . Geometry of a swept laminated wing

2.1. Classical plate theory (CPT)
In CPT, the displacement field of a plate is given in [15] and can be expressed as:

$$u_x(x,y,z,t) = u_{x_0}(x,y,t) - z\frac{\partial w_{z_0}(x,y,t)}{\partial x} \tag{1}$$

$$v_y(x,y,z,t) = v_{y_0}(x,y,t) - z\frac{\partial w_{z_0}(x,y,t)}{\partial y} \tag{2}$$

$$w_z(x,y,z,t) = w_{z_0}(x,y,t) \tag{3}$$

According to the kinematic hypotheses, the strain–displacement relationships for a plate can be written as:

$$\varepsilon_x = \frac{\partial u_{x_0}}{\partial x} - z\frac{\partial^2 w_{z_0}}{\partial x^2} \tag{4}$$

$$\varepsilon_y = \frac{\partial v_{y_0}}{\partial y} - z\frac{\partial^2 w_{z_0}}{\partial y^2} \tag{5}$$

$$\gamma_{xy} = \frac{\partial u_{x_0}}{\partial y} + \frac{\partial v_{y_0}}{\partial x} - 2\,z\frac{\partial^2 w_{z_0}}{\partial x \partial y} \tag{6}$$

The relationships between the applied forces and moments and the resulting mid-plane strains and curvatures for a general laminate are expressed in matrix form as follows:

$$\left\{ \begin{array}{c} N \\ M \end{array} \right\} = \left[\begin{array}{cc} A & B \\ B & D \end{array} \right] \left\{ \begin{array}{c} \varepsilon \\ K \end{array} \right\} \tag{7}$$

where force and moment per unit length are denoted by N and M, respectively. The extensional stiffness matrix, the coupling stiffness matrix, and the bending stiffness matrix are represented by the matrices $[A]$, $[B]$, and $[D]$, respectively. The mid-plane strain vector is $[\varepsilon]$, while the curvature strain vector is $[K]$. The values of $[B]$ in a symmetric laminate are zero, meaning that there is no direct coupling between in-plane forces and bending moments. Therefore,

$$\left\{ \begin{array}{c} M_x \\ M_y \\ M_{xy} \end{array} \right\} = \left[\begin{array}{ccc} D_{11} & D_{12} & D_{16} \\ D_{21} & D_{22} & D_{26} \\ D_{61} & D_{62} & D_{66} \end{array} \right] \left\{ \begin{array}{c} K_x \\ K_y \\ K_{xy} \end{array} \right\} \tag{8}$$

2.2. Orthotropic composite elastic behavior
From the stress-strain relationships for an orthotropic material [16], the stiffness components, D_{ij}, for an n-ply laminate with arbitrary ply angle orientations can be given as:

$$D_{ij} = \frac{1}{3}\sum_{k=1}^{n} \left[\bar{Q}_{ij}\right]_k (z_k^3 - z_{k-1}^3) \tag{9}$$

2.3. General Rayleigh-Ritz formulation

The fundamental frequencies are obtained by applying the Rayleigh-Ritz method formulation. As stated in [2] and [17], the wing transverse deflection can be represented as:

$$w = \sum_{i=1}^{4} \gamma_i(x, y) q_i(t) \tag{10}$$

where $q_i(t)$ represents the Rayleigh-Ritz generalized displacements, and $\gamma_i(x, y)$ represents the assumed mode modes, expressed as:

$$\gamma_i(x, y) = \phi_i(x)\psi_i(y) \tag{11}$$

The mode shapes, $\phi_i(x)$ in x-direction and $\psi_i(y)$ in y-direction, are defined according to [18] and are shown in Fig. 2.

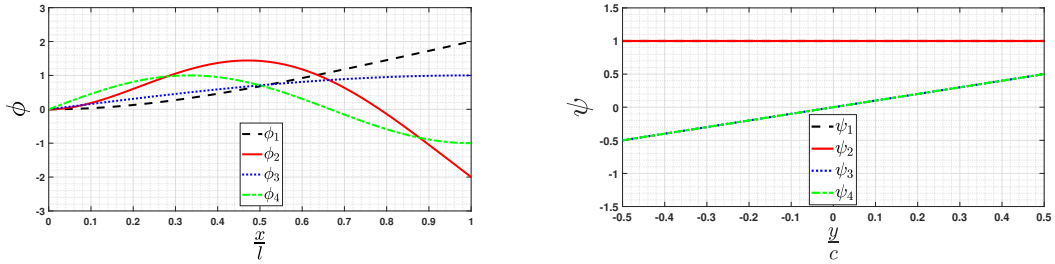

(a) (b)

Figure 2 . Mode shapes of the rectangular composite wing: (a) In the x-direction $\phi_i(x)$, and (b) In the y-direction $\psi_i(y)$.

The equation for the transverse deflection of wings is rewritten as follows:

$$w = h + \bar{y}\alpha \tag{12}$$

where

$$h = \phi_1 q_1 + \phi_2 q_2 \tag{13}$$

$$\alpha = \frac{1}{c}(\phi_3 q_3 + \phi_4 q_4)\cos\Lambda - (\frac{d\phi_1}{d\bar{x}} q_1 + \frac{d\phi_2}{d\bar{x}} q_2)\sin\Lambda \tag{14}$$

The plunge and pitch deflections are represented by h and α, respectively, as shown in Fig. 3.

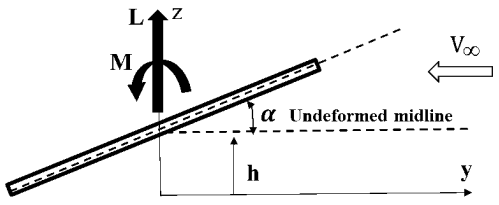

Figure 3 . Force-Moment-deflection diagram of swept laminated wing, illustrating plunge h and pitch α deflections.

2.4. Lagrange Equation

According to [17], Lagrange's equation is based on three key components: kinetic energy (T), potential energy (V), and generalized force (Q_i), which represents the virtual work performed by external forces (δW_{ext}). It is expressed as follows:

$$\frac{d}{dt}(\frac{\partial T}{\partial \dot{q}_i}) + \frac{\partial V}{\partial q_i} - \frac{\partial T}{\partial q_i} = Q_i \tag{15}$$

2.4.1. Kinetic energy equation : It represents energy related to the motion of the plate and the limits of integration of the swept wing are considered using $\ell = \frac{l}{\cos\Lambda}$, $x = \bar{x}\cos(\Lambda)$, and $y = \bar{y}$, hence:

$$T = \frac{1}{2}\cos(\Lambda)\int_0^{\ell}\int_{-\frac{c}{2}}^{\frac{c}{2}} m\dot{w}^2 \, d\bar{y} \, d\bar{x} \tag{16}$$

Where t is the wing thickness, m is the wing mass $m = \rho \cdot t$, and ρ is the wing specific gravity (density per unit area). The first term of (15) can be expressed algebraically as follows by substituting (12) into (16), differentiating w.r.t q_i, and assuming a harmonic motion $q_i = \bar{q}_i e^{i\omega t}$, hence:

$$\frac{d}{dt}\left(\frac{\partial T}{\partial \dot{q}_i}\right) = -\omega^2[\mathrm{M}]\{\bar{q}_i\}e^{i\omega t} \tag{17}$$

2.4.2. Potential energy equation : It defines the energy stored in the laminated wing because of its position [18] and assumes that no forces act in the x and y directions. Hence, after simplification, it can be expressed as follows:

$$\begin{aligned} V = \frac{1}{2}\cos\Lambda\int_0^{\ell}\int_{-\frac{c}{2}}^{\frac{c}{2}} \big[D_{11}{w_{xx}}^2 + 2D_{12}w_{xx}w_{yy} + D_{22}{w_{yy}}^2 \\ +4D_{16}w_{xx}w_{yy} + 4D_{26}w_{yy}w_{xy} + 4D_{66}{w_{xy}}^2\big)\, d\bar{y}d\bar{x} \end{aligned} \tag{18}$$

The final matrix form can be expressed as follows by substituting (12) into (18) and differentiating (18) w. r. t. q_i, hence:

$$\frac{\partial V}{\partial q_i} = [\mathrm{K}]\{\bar{q}_i\}e^{i\omega t} \tag{19}$$

2.4.3. External work equation : The generalized forces, which represent the changes in the external forces on the plate according to [1, 17], are stated below:

$$\delta W_{ext} = \cos\Lambda\int_0^{\ell}\int_{-\frac{c}{2}}^{\frac{c}{2}} \Delta p_z \delta w d\bar{y}d\bar{x} \tag{20}$$

where Δp_z represents the distributed lateral load per unit area. Eq. 20 can be decomposed as follows:

$$\delta\mathrm{W}_{ext} = Q_1\delta q_1 + Q_2\delta q_2 + Q_3\delta q_3 + Q_4\delta q_4 \tag{21}$$

where

$$Q_1 = \cos\Lambda\int_0^{\ell} L\phi_1 d\bar{x} - \cos\Lambda\sin\Lambda\int_0^{\ell} M_a\frac{d\phi_1}{d\bar{x}}d\bar{x} \tag{22}$$

$$Q_2 = \cos\Lambda\int_0^{\ell} L\phi_2 d\bar{x} - \cos\Lambda\sin\Lambda\int_0^{\ell} M_a\frac{d\phi_2}{d\bar{x}}d\bar{x} \tag{23}$$

$$Q_3 = -\frac{\cos\Lambda^2}{c}\int_0^{\ell} M_a\phi_3 d\bar{x},\ Q_4 = -\frac{\cos\Lambda^2}{c}\int_0^{\ell} M_a\phi_4 d\bar{x} \tag{24}$$

The relations for 2D incompressible unsteady aerodynamic flow were derived by Spielberg [19] and adapted for the swept plate as described in [17]. The generalized forces, as previously shown in Fig. 3 where aerodynamic lift is denoted by L and moment by M_a, can be written as:

$$\mathrm{L} = \pi\rho\mathrm{b}^3\omega^2\cos\Lambda\left[\mathrm{L_h}\frac{\mathrm{h}}{\mathrm{b}} + \mathrm{L}_\alpha\alpha\right]\mathrm{e}^{\mathrm{i}\omega\mathrm{t}} \tag{25}$$

$$M_a = \pi\rho\mathrm{b}^4\omega^2\cos\Lambda\left[\mathrm{M_h}\frac{\mathrm{h}}{\mathrm{b}} + \mathrm{M}_\alpha\alpha\right]\mathrm{e}^{\mathrm{i}\omega\mathrm{t}} \tag{26}$$

where

$$L_h = 1 - 2i\frac{C(k)}{k}, \quad L_\alpha = \frac{i}{k} + 2\frac{C(k)}{k^2} + i\frac{C(k)}{k} \tag{27}$$

$$M_h = -i\frac{C(k)}{k}, \quad M_\alpha = \frac{1}{8} - \frac{i}{2k} + \frac{C(k)}{k^2} + i\frac{C(k)}{2k} \tag{28}$$

The lift and moment coefficients, L_h, L_α, M_h, and M_α, are caused by changes in the plunge (h) and pitch (α) deflections, respectively.

Where the R. T. Jones approximation for the Theodorsen function, denoted by $C(k)$, is written as follows:

$$C(k) = \frac{0.5P^2 + 0.2808P + 0.01365}{P^2 + 0.3455P + 0.01365} \tag{29}$$

where $P = ik$ and k is the reduced frequency. The final matrix form is obtained by substituting Equations (13), (14), (22), (23), (24), (25), and (26) into the appropriate equations, as stated below:

$$Q_i = \pi\rho b^3\omega^2 \left[A\right] \left\{\bar{q}_i\right\} e^{i\omega t} \tag{30}$$

Finally, substitute Equations (17), (19), and (30) into Lagrange's equation. This yields:

$$(-\omega^2[\mathrm{M}] + [\mathrm{K}])\{\bar{q}_i\}e^{i\omega t} = \pi\rho b^3\omega^2[A]\{\bar{q}_i\}e^{i\omega t} \tag{31}$$

2.5. Free vibration analysis

By setting the generalized forces (Q_i) to zero on the right-hand side in matrix form (31), the four natural frequencies (first bending, first torsion, second bending, and second torsion) can be obtained. This involves setting the determinant of the resulting eigenvalue problem to zero and extracting the eigenvalues. The natural frequencies are then calculated as the square root of each eigenvalue.

2.6. Aero-elastic analysis

After obtaining natural frequencies, an aeroelastic analysis is performed to determine the divergence and flutter velocities of the composite wings.

2.6.1. Flutter analysis : The V-g method is used to analyze structural stability through damping. Positive structural damping indicates instability, while negative damping indicates that the structure is stable. Flutter occurs when the actual damping of the structure matches the structural damping coefficient, g.

The matrix form in Equation (31) is simplified and rearranged as:

$$\mathrm{Z}\ [\mathrm{K}] - [\mathrm{B}] = 0 \tag{32}$$

Where the complex eigenvalue (Z) and [B] can be respectively represented as: $\mathrm{Z} = \frac{(1+\mathrm{ig})}{\omega^2}$, and $[B] = \pi\rho b^3[\mathrm{A}] + [\mathrm{M}]$. The equation of motion can be solved at a specified value of the reduced frequency (κ).This leads to four complex eigenvalues, denoted as Z_i. For each complex eigenvalue (Z_i), the corresponding natural frequency (ω) and structural damping (g) can be determined using the following relationships: $\omega = \frac{1}{\sqrt{\mathrm{Re}(Z)}}$, and $g = \frac{\mathrm{Im}(Z)}{\mathrm{Re}(Z)}$. The airspeed ($V$) can then be calculated using the following equation: $V = \frac{b\omega}{\kappa}$.

By repeating this process for a range of reduced frequency values, the V-g diagram can be generated. This diagram plots the structural damping (g) against the airspeed (V) for each eigenvalue.

Flutter occurs when the structural damping (g) becomes zero. The corresponding airspeed at this point is the flutter speed (V_F), and the associated frequency is the flutter frequency (ω_F).

2.6.2. Divergence analysis : It is computed using the V-g diagram, in which the V-g branch, without exceeding the V-axis, goes from a negative value to zero. The V-ω diagram, in which the V-ω branch goes to zero frequency, is the clearest from the V-g diagram.

3. RESULTS AND DISCUSSION

3.1. Free vibration analysis

3.1.1. Straight wings : The analytical and numerical analysis is evaluated using MATLAB code and NASTRAN software to validate the current analysis. In the finite element model, a CQUAD4 quadrilateral shell element with a size of 2 mm is utilized, resulting in a mesh with 5776 elements and 5967 nodes. In the current research, the material properties and dimensions used are presented by S. J. Hollowell et al. [1]. A variety of laminates are investigated to confirm that the current model is applicable for a broad range of bending-torsion coupling stiffness. The flexural moduli (D_{ij}) of the various layers of the laminated composite plates used in this study and subsequent subsections are presented in Table 1. The results of the present model (Pres.), the finite element model (FEM), and the experimental results (Exp.) are compared in Table 2, with allowable differences (Diff%).

Table 1 . Flexural modulus of the straight laminated wing.

Lamination	D_{11}	D_{12}	D_{22}	D_{16}	D_{26}	D_{66}
$[0_2/90]_s$	5.473	0.128	0.651	0	0	0.260
$[\pm 45/0]_s$	1.996	1.291	1.803	0.579	0.579	1.422
$[+45_2/0]_s$	1.996	1.291	1.803	1.254	1.254	1.422
$[-45_2/0]_s$	1.996	1.291	1.803	-1.254	-1.254	1.422
$[+30_2/0]_s$	3.541	1.000	0.840	1.589	0.583	1.132
$[-30_2/0]_s$	3.541	1.000	0.840	-1.589	-0.583	1.132

In Table 1, the laminate $[0_2/90]_s$ is the only uncoupled example and exhibits the maximum bending stiffness, D_{11}, with zero bending-torsion coupling stiffness coefficients, D_{16} and D_{26}. The maximum torsional stiffness, D_{66}, is demonstrated by the three laminates $[\pm 45_2/0]_s$, $[+45_2/0]_s$, and $[-45_2/0]_s$; however, , except for the laminate $[\pm 45_2/0]_s$, they still show significant values for D_{16} and D_{26}. The maximum bending-torsion coupling stiffness, D_{16}, and significant bending stiffness, D_{11}, are exhibited by the two laminates $[+30_2/0]_s$ and $[-30_2/0]_s$. Notably, as illustrated in Fig.4, the flexural modulus of laminate $[-\theta_2/0]_s$ and laminate $[+\theta_2/0]_s$ are the same, with the only difference being the signs of D_{16}.

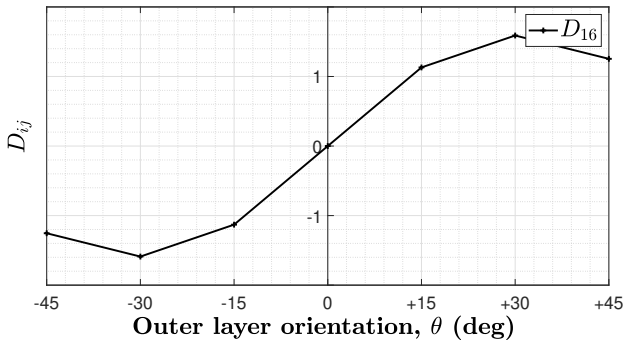

Figure 4 . Flexural modulus of the laminate $[\theta_2/0]_s$.

Table 2 . Natural frequencies of the straight laminated wing.

Lamination	Mode shapes	Pres.	FEM	REF. [1]	Diff.%	
					Pres. with FEM	Pres. with [1]
$[0_2/90]_s$	1B	12.747	12.73	12.7	0.13	0.37
	1T	35.533	41.76	34.4	-14.91	3.29
	2B	79.885	79.753	79.8	0.17	0.11
	2T	130.861	142.32	-	-8.05	-
$[\pm 45/0]_s$	1B	7.231	6.303	7.25	14.72	-0.26
	2B	45.743	39.111	47.9	16.96	-4.5
	1T	80.850	79.018	80.6	2.32	0.31
	2T	246.611	$226.47{,}5^{th}$	-	8.89	-
$[+45_2/0]_s$& $[-45_2/0]_s$	1B+1T	5.162	5.388	5.23	-4.20	-1.30
	2B+1T	35.508	33.307	46.8	6.61	-24.13
	1T	81.538	55.243	81.4	47.60	0.17
	2T	248.119	$168.4{,}5^{th}$	-	47.34	-
$[+30_2/0]_s$& $[-30_2/0]_s$	1B+1T	6.288	6.906	6.35	-8.95	-0.98
	2B+1T	44.292	41.063	59.7	7.86	-25.81
	1T	74.548	64.734	75.9	15.16	-1.78
	2T	228.943	$197.05{,}5^{th}$	-	16.19	-

Table 2, except for the laminate $[0_2/90]_s$, all the laminated models have the first bending mode (1B) as the smallest frequency, followed by the second bending (2B), first torsion (1T), and second torsion (2T), respectively, as shown in Figs. 5b, c, d. As seen in Fig. 5a, the first torsion (1T) and second bending (2B) modes switch places for the cross-ply laminate because of the clear bending-torsion decoupling. This decoupling results from the absence of significant off-axis stiffness contributions, which allows the bending and torsion modes to behave independently.

Due to the significant values of coupling stiffnesses D_{16} and D_{26} for the laminate $[+45_2/0]_s$, which produce the frequency disparities, the first two natural frequencies of the laminate $[+45_2/0]_s$ are lower than those of the laminate $[\pm 45/0]_s$. This is because the stiffness coupling alters the structural response, reducing the overall stiffness and shifting the natural frequencies. The bending and torsion frequencies of the laminated models are highly sensitive to this coupling, as demonstrated by the frequency disparities in the results.

Figure 5 visually illustrates these effects by showing the mode shapes (1B, 1T, 2B, 2T) for different laminates, such as $[0_2/90]_s$, $[\pm 45/0]_s$, $[+45_2/0]_s$, and $[+30_2/0]_s$. It highlights how bending-torsion coupling influences the mode shapes. For instance, laminates with positive coupling (e.g., $[+45_2/0]_s$) exhibit coupled modes (e.g., 1B+1T), where bending and torsion deformations occur simultaneously. In contrast, laminates with negative coupling (e.g., $[-45_2/0]_s$) show distinct bending and torsion modes, as the coupling stiffness causes the deformations to work against each other. This figure helps visualize the stiffness anisotropy and its impact on the structural dynamics of the wing.

A notable observation is that the second bending mode (2B) coupling with the first torsion mode (1T) in the laminates $[+\theta_2/0]_s$ and $[-\theta_2/0]_s$ differs from Ref. [1]. This discrepancy arises because Ref. [1] used a three-term deflection model, whereas the finite element method (FEM) employed in this study can more accurately capture the coupled mode behavior. Additionally, the unbalanced laminates $[+\theta_2/0]_s$ and $[-\theta_2/0]_s$ exhibit significant discrepancies in the first torsion (1T) and second torsion (2T) modes, as the FEM accounts for transverse shear deformation and warping effects, which are ignored by Classical Lamination Theory (CLT). These effects are particularly important in torsion-related modes and are more adequately represented in finite element models.

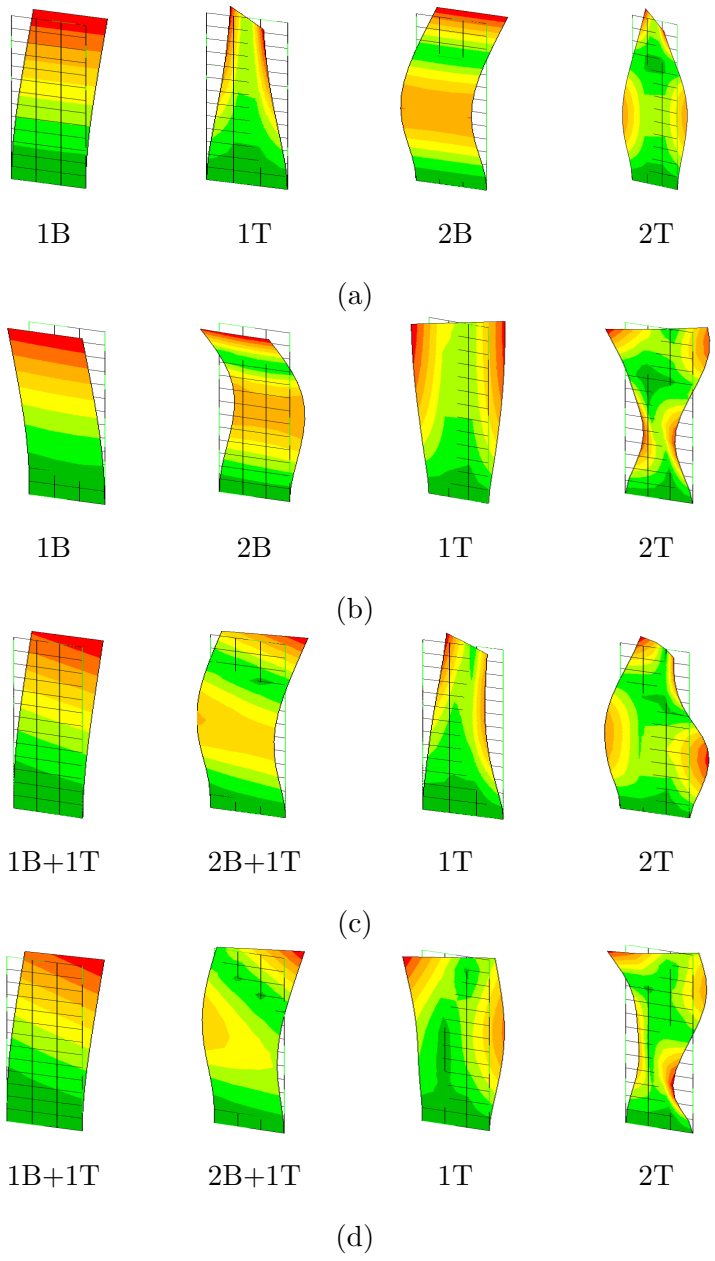

Figure 5 . Mode shapes of the straight laminated plate: (a) $[0_2/90]_s$, (b) $[\pm 45/0]_s$, (c) $[+45_2/0]_s$ & $[-45_2/0]_s$, and (d) $[+30_2/0]_s$ & $[-30_2/0]_s$.

3.1.2. Swept wings : Swept-forward wing is represented by negative angles, and the swept-back wing is represented by positive angles. The present results of swept wings are illustrated in Table 3.

Table 3 . Natural frequencies of the swept laminated wing.

Lamination	Mode shapes	$\Lambda = 0°$	$\Lambda = 10°$	$\Lambda = 20°$	$\Lambda = 30°$
$[0_6]$	$1B$	12.970	12.580	11.464	9.776
	$1T$	34.466	35.572	34.466	31.291
	$2B$	78.707	81.281	78.707	69.918
	$2T$	127.012	131.731	127.012	113.660
$[+15_2/0]_s$& $[-15_2/0]_s$	$1B$	9.036	8.756	7.959	6.765
	$1T$	47.049	48.499	47.049	42.791
	$2B$	62.978	65.581	62.978	54.852
	$2T$	168.721	174.304	168.721	152.490
$[+30_2/0]_s$& $[-30_2/0]_s$	$1B$	6.289	6.095	5.544	4.717
	$2B$	42.416	44.292	42.416	36.619
	$1T$	72.154	74.548	72.154	65.244
	$2T$	221.893	228.944	221.893	201.454
$[+45_2/0]_s$& $[-45_2/0]_s$	$1B$	5.162	5.005	4.558	3.884
	$2B$	34.046	35.508	34.046	29.470
	$1T$	79.031	81.538	79.031	71.804
	$2T$	240.554	248.119	240.554	218.712

The results presented in Tables 3 and Figure 6 demonstrate a consistent trend: the natural frequencies of the laminated models decrease with increasing sweep angle (Λ), regardless of whether it is forward or backward sweep. This behavior can be attributed to the reduction in structural stiffness as the sweep angle increases. When a wing is swept, the effective spanwise stiffness decreases because the load path becomes less direct, leading to a reduction in natural frequencies. This is particularly evident in the bending modes, where the wing's ability to resist deformation is diminished due to the sweep-induced geometric changes.

Figure 6: Natural Frequencies of Swept Laminated Plates visually illustrates this trend by plotting the natural frequencies of swept laminated wings as a function of the sweep angle (Λ). The figure shows that increasing the sweep angle reduces the natural frequencies, with laminates exhibiting higher off-axis stiffness (e.g., $[+45_2/0]_s$) displaying different trends compared to those with minimal coupling (e.g., $[0_6]$). This highlights the influence of stiffness anisotropy on the frequency characteristics of swept wings.

The influence of the outer layer orientation angle (θ) on the frequency characteristics is further explored in Figure 7: Natural Frequencies of Outer Layer Orientation Angle (θ). This figure shows how the natural frequencies vary with θ for different sweep angles. It reveals that laminates with positive orientations (e.g., $[+30_2/0]_s$) have higher frequencies compared to those with negative orientations (e.g., $[-30_2/0]_s$). This is due to the stiffness coupling introduced by the off-axis plies, which alters the structural response to dynamic loading. As θ increases, the coupling between bending and torsion becomes more pronounced due to the increased D_{16} and D_{26} terms in the flexural stiffness matrix. This coupling causes a shift in the mode order, where the first torsion mode (1T) occurs after the second bending mode (2B). This phenomenon is a direct result of the stiffness anisotropy introduced by the off-axis plies, which alters the structural response to dynamic loading.

For laminates with lower outer layer orientation angles, such as $[0_6]$ and $[+15_2/0]_s$, the mode order remains consistent: first bending (1B), first torsion (1T), second bending (2B), and then second torsion (2T). This is because these laminates exhibit minimal bending-torsion coupling, and their stiffness is dominated by the axial and transverse stiffness components (D_{11} and D_{22}). The absence of significant off-axis stiffness contributions ensures that the natural frequencies follow the expected order for a decoupled system.

The observed discrepancies between the present model and the finite element results, particularly for the first torsion (1T) and second torsion (2T) modes, can be explained by the limitations of Classical Lamination Theory (CLT). CLT does not account for transverse shear deformation, which becomes increasingly important in torsion-related modes. Additionally, warping effects, which are more accurately captured by finite element models, are not considered in the present analytical model. These factors contribute to the differences in the higher-order modes, especially for laminates with significant bending-torsion coupling.

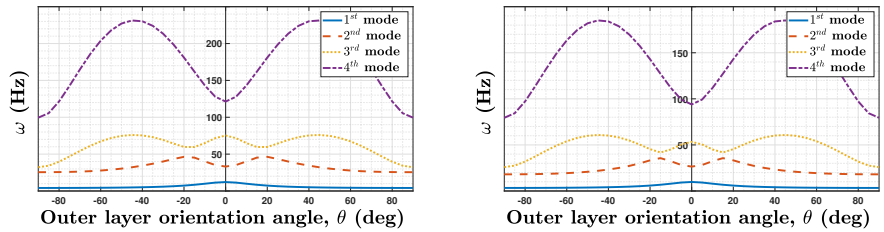

(a) $\Lambda = 15^\circ$ & $\Lambda = -15^\circ$ (b) $\Lambda = 30^\circ$ & $\Lambda = -30^\circ$

Figure 6 . Natural frequencies of swept laminated plates.

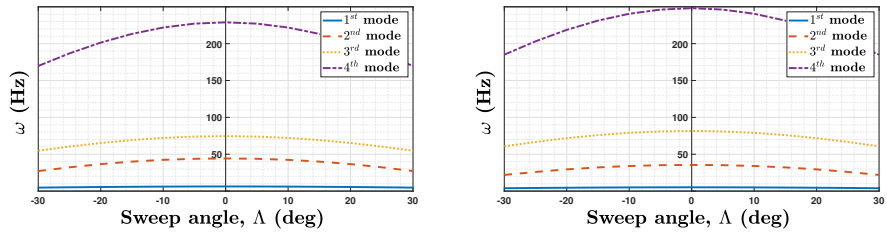

(a) $[+30_2/0]_s$ & $[-30_2/0]_s$ (b) $[+45_2/0]_s$ & $[-45_2/0]_s$

Figure 7 . Natural frequencies of outer layer orientation angle θ.

3.2. Aeroelastic analysis

3.2.1. Straight wings : The flutter and divergence speeds of the straight laminated wing were compared with those reported in the literature (Refs. [1, 12, 13]), as summarized in Table 4. The flutter and divergence speeds for the straight laminated wing were determined by analyzing V-g curves, as illustrated in Fig. 8.

Table 4 . Flutter and divergence speeds and frequencies of the straight laminated wing.

Lamination	Present			Ref [1]			Ref [18]		Ref [19]	
	V_D	V_F	ω_F	V_D	V_F	ω_F	V_D	V_F	V_D	V_F
$[0_2/90]_s$	20.11	18.58^{2nd}	23.24	22.3	21	25	30.6	23	25.4	26.4
$[\pm 45/0]_s$	–	42.58^{2nd}	39.6	–	39	39	–	40.1	–	47.5
$[+45_2/0]_s$	–	36.05^{2nd}	31.5	–	27.8	28	–	27.5	–	27.8
$[-45_2/0]_s$	10.25	47.99^{3rd}	47.48	9.9	27.8	27	13.7	27.8	12.7	29.1
$[+30_2/0]_s$	–	30.98^{2nd}	33.65	–	27.8	31	–	27.1	–	27.4
$[-30_2/0]_s$	9.69	49.95^{3rd}	39.93	10.2	30	29	13.8	37.3	12.8	48.1

The analysis of Tables 1 and 4 reveals a strong correlation between bending-torsion coupling stiffness and aeroelastic stability. The underlying structural mechanics and material behavior of the laminated wings can explain the observed trends.

Figure 8: V-ω & V-g Curves of the Straight Laminated Wing presents the V-ω (frequency vs. airspeed) and V-g (damping vs. airspeed) curves for straight laminated wings. These curves are used to determine the flutter and divergence speeds by identifying the points where damping becomes negative (flutter) or the frequency drops to zero (divergence). The curves show how the bending-torsion coupling and outer layer orientation influence the aeroelastic stability of the wing. For example, laminates with positive bending-torsion coupling stiffness values (D_{16} and D_{26}), such as $[+\theta_2/0]_s$ and $[\pm\theta/0]_s$, exhibit divergence-free behavior. This is because the positive coupling enhances the structural stability of the wing by aligning the bending and torsional deformations in a way that delays the onset of divergence. Flutter in these laminates typically occurs in the second bending mode (2B), as evidenced by the V-g curves for laminates $[\pm 45/0]_s$, $[+45_2/0]_s$, and $[+30_2/0]_s$ in Figs. 8b, c, and e. This behavior results from the stiffness anisotropy introduced by the off-axis plies, which increases the torsional rigidity and delays the onset of flutter.

Conversely, laminates with negative bending-torsion coupling stiffness, such as $[-45_2/0]_s$ and $[-30_2/0]_s$, exhibit divergence occurring before flutter. This is because the negative coupling reduces the structural stability of the wing, making it more susceptible to divergence at lower airspeeds. In these cases, divergence typically occurs in the first bending mode (1B), while flutter occurs later in the third

mode (1T), as observed in Figs. 8a, d, and f. The negative coupling causes the bending and torsional deformations to work against each other, reducing the overall stiffness and making the wing more prone to aeroelastic instabilities.

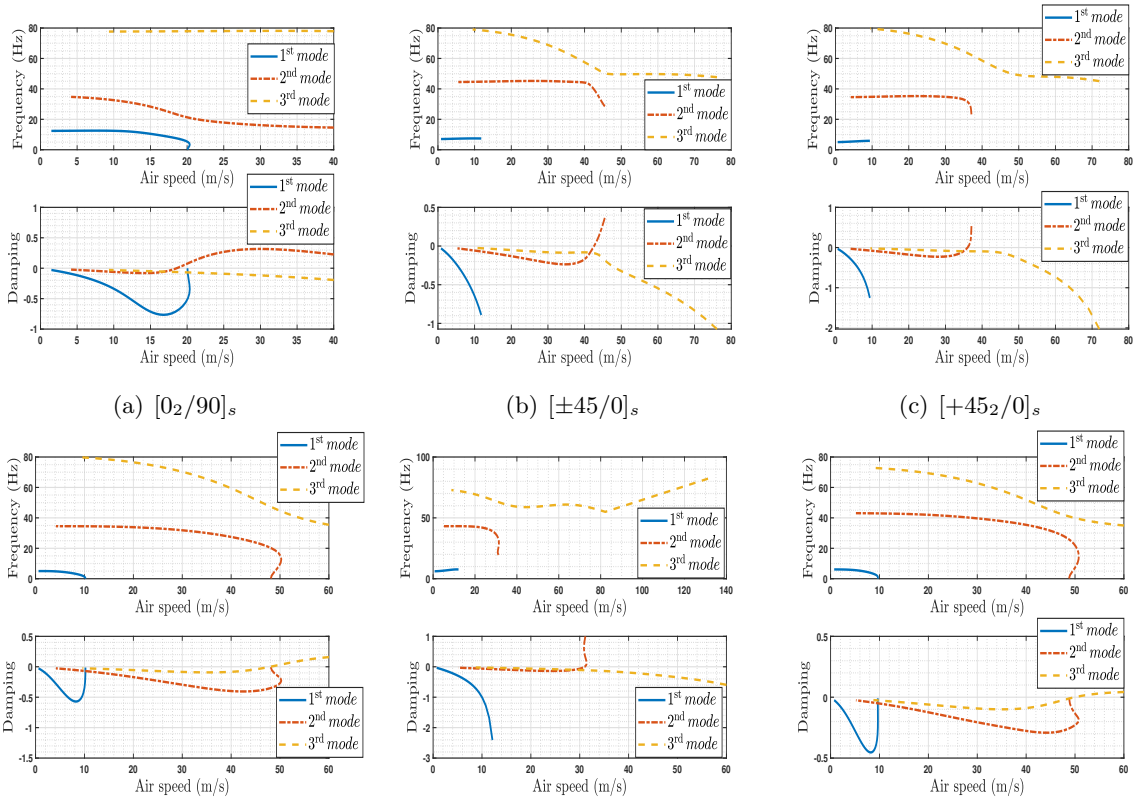

(a) $[0_2/90]_s$ (b) $[\pm 45/0]_s$ (c) $[+45_2/0]_s$

(d) $[-45_2/0]_s$ (e) $[+30_2/0]_s$ (f) $[-30_2/0]_s$

Figure 8 . V-ω & V-g curves of the straight laminated wing.

3.2.2. Swept wings : The flutter and divergence speeds are obtained as presented in Table 5.

Table 5 . Flutter and divergence speeds of the swept laminated wing at various sweep angles.

Sweep angle	Speeds	$[-45_2/0]_s$	$[-30_2/0]_s$	$[-15_2/0]_s$	$[0_2/0]_s$	$[+15_2/0]_s$	$[+30_2/0]_s$	$[+45_2/0]_s$
$\Lambda = -30°$	V_D	6.004	6.339	7.771	14.015	No	No	22.114
	V_F	37.087^{3rd}	33.838^{3rd}	18.758^{3rd}	17.454^{2nd}	24.275^{2nd}	31.445^{2nd}	34.957^{3rd}
$\Lambda = -20°$	V_D	7.145	7.375	8.861	15.990	No	No	No
	V_F	45.254^{3rd}	47.572^{3rd}	37.771^{2nd}	18.755^{2nd}	24.805^{2nd}	32.003^{2nd}	42.069^{3rd}
$\Lambda = -10°$	V_D	8.501	8.488	9.917	18.007	No	No	No
	V_F	48.241^{3rd}	51.230^{3rd}	36.498^{2nd}	18.689^{2nd}	24.436^{2nd}	32.855^{2nd}	39.029^{2nd}
$\Lambda = 0°$	V_D	10.246	9.687	10.890	20.128	No	No	No
	V_F	47.989^{3rd}	49.953^{3rd}	37.634^{2nd}	18.565^{2nd}	23.348^{2nd}	30.985^{2nd}	36.050^{2nd}
$\Lambda = 10°$	V_D	12.949	11.044	11.747	22.608	No	No	No
	V_F	44.338^{3rd}	41.638^{3rd}	39.467^{2nd}	17.907^{2nd}	22.391^{2nd}	28.612^{2nd}	31.973^{2nd}
$\Lambda = 20°$	V_D	19.544	12.765	12.463	26.342	No	No	No
	V_F	39.377^{3rd}	34.469^{3rd}	36.210^{2nd}	16.610^{2nd}	21.110^{2nd}	23.998^{2nd}	26.053^{2nd}
$\Lambda = 30°$	V_D	No	15.473	12.986	30.899	No	No	No
	V_F	34.692^{3rd}	30.135^{3rd}	16.061^{3rd}	15.205^{2nd}	18.458^{2nd}	20.632^{2nd}	22.376^{2nd}

Table 5 illustrates the variation of flutter and divergence speeds with sweep angle (Λ) for various laminated models.The flutter speeds for the laminates $[-45_2/0]_s$, $[-30_2/0]_s$, and $[0_6]$ consistently decrease

as the sweep angle increases. For the laminates $[-45_2/0]_s$ and $[-30_2/0]_s$, the flutter speeds are associated with the third mode shape (1T). In the case of the laminate $[-15_2/0]_s$, the flutter speeds correspond to the second mode shape (1T) when the sweep angle is in the range of $-20° < \Lambda < 20°$. However, at sweep angles outside this range ($-20° > \Lambda$ and $\Lambda > 20°$), the flutter speeds are linked to the third mode shape (2B). For the laminate $[0_6]$, the flutter speeds are also associated with the second mode shape (1T).

For the laminates $[+45_2/0]_s$, $[+30_2/0]_s$, and $[+15_2/0]_s$, the flutter speeds decrease as the sweep-back angle increases, while they increase as the sweep-forward angle increases. The flutter speeds relate to the second mode shape (1T) for the laminate $[+15_2/0]_s$, and they correspond to the second mode shape (2B) for the laminates $[+45_2/0]_s$ and $[+30_2/0]_s$ as shown in Fig. 9a. The laminates $[-45_2/0]_s$, $[-30_2/0]_s$, $[-15_2/0]_s$, and $[0_6]$ exhibit slight increases in divergence speed as the sweep angle (Λ) becomes more positive, particularly when Λ exceeds 0°. In contrast, the laminates $[+45_2/0]_s$, $[+30_2/0]_s$, and $[+15_2/0]_s$ show slight increases in divergence speed as the sweep angle becomes more negative, especially at $\Lambda < 0°$.

Furthermore, divergence speeds are generally higher for laminates with positive outer ply orientations ($[+45_2/0]_s$, $[+30_2/0]_s$, and $[+15_2/0]_s$) compared to those with negative outer ply orientations ($[-45_2/0]_s$, $[-30_2/0]_s$, and $[-15_2/0]_s$), as illustrated in Fig. 9b.

Referring to Tables 5, the flutter and divergence speeds are a function of the outer layer orientation angle for various sweep angles. The results provide insight into how flutter speeds vary with changes in the outer layer orientation and sweep angle. The flutter speeds are highly sensitive to outer layer orientation angles, with significant variations depending on the orientation. Sweep-forward angles ($\Lambda < 0°$) tend to result in higher peak flutter speeds compared to sweep-back angles as shown in Fig.10a.

Divergence speeds are generally lower and less sensitive to outer layer orientation angles at sweep forward angles and are higher at sweep back angles. Positive orientation angles ($\theta > 0$) generally result in higher divergence speeds compared to negative orientations ($\theta < 0$) as shown in Fig. 10b.

Due to the high bending-torsion coupling of the laminates $[+\theta_2/0]_s$, flutter speeds decrease as the sweep-back angle increases, while they increase as the sweep-forward angle increases. Additionally, a divergence-free wing is observed, as shown in Fig. 11. Specifically, as the sweep angle increases, the flutter speeds for the laminate $[\theta_2/0]_s$ decrease. In contrast, the divergence speeds increase with a larger sweep-back angle and decrease with a larger sweep-forward angle, as illustrated in Fig. 12.

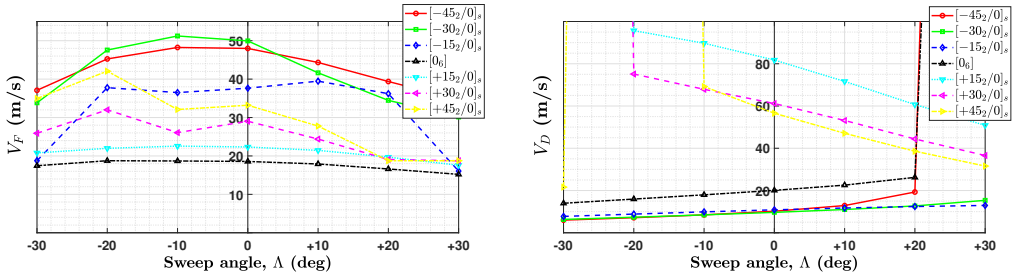

(a) Flutter speed vs. sweep angle. (b) Divergence speed vs. sweep angle.

Figure 9 . Variation of flutter and divergence speeds with sweep angle.

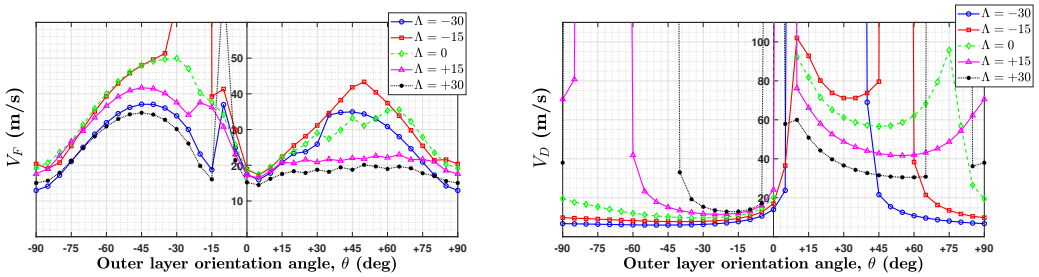

(a) Flutter speed vs. outer layer orientation. (b) Divergence speed vs. outer layer orientation.

Figure 10 . Variation of flutter and divergence speeds with outer layer orientation angle.

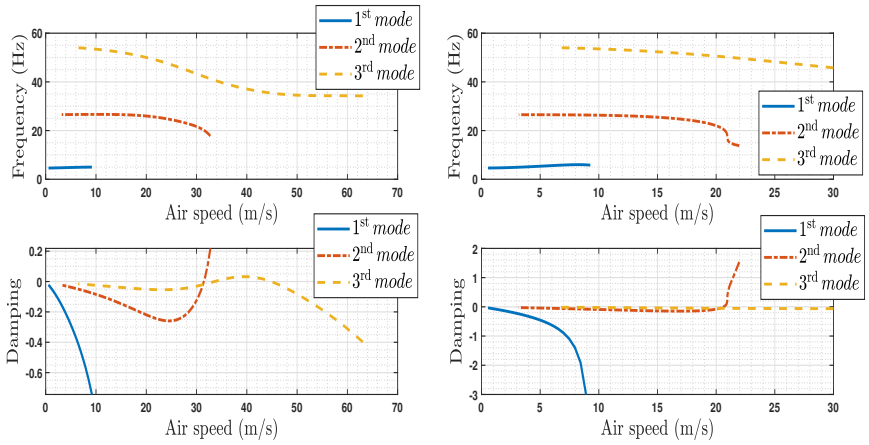

(a) $\Lambda = -30$ (b) $\Lambda = 30$

Figure 11 . Flutter and divergence speeds of the laminate $[+30_2/0]_s$.

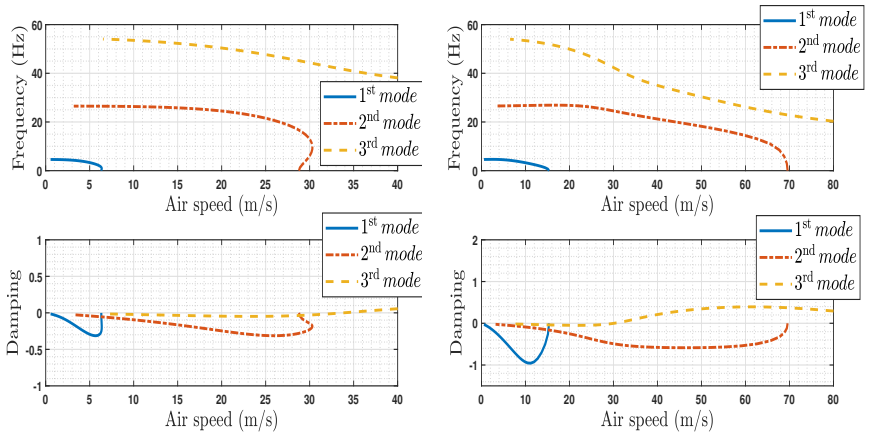

(a) $\Lambda = -30$ (b) $\Lambda = 30$

Figure 12 . Flutter and divergence speeds of the laminate $[-30_2/0]_s$.

4. Conclusion

This study investigated the aeroelastic behavior of swept composite wings, focusing on flutter and divergence. Key findings include the significant influence of bending-torsion coupling stiffness on aeroelastic stability. Negative coupling can lead to divergence occurring before flutter, while positive coupling can effectively increase the divergence speed. Furthermore, increasing the sweepback angle generally increases divergence speed. The proposed analytical model provides a time-efficient alternative to finite element methods for analyzing these critical aeroelastic phenomena. These findings have significant implications for aircraft design, enabling the optimization of composite wing structures through tailored layup schedules to enhance aeroelastic stability and performance.

5. References

[1] Hollowell S J, Dugundji J 1984 Aeroelastic flutter and divergence of stiffness coupled, graphite/epoxy cantilevered plates Journal of Aircraft 21(1) 69–76.
[2] Lottati I 1985 Flutter and divergence aeroelastic characteristics for composite forward swept cantilevered wings Journal of Aircraft 22 1001–1007.
[3] Attaran A, Majid D L, Basri S, Rafie A S M, Abdullah E J 2008 Structural optimization of an aero-elastically tailored composite flat plate made of woven fiberglass/epoxy Acta Mechanica 196(3–4) 161–173.
[4] Bach, C., Jebari, R., Viti, A., & Hewson, R. (2017). Composite stacking sequence optimization for aeroelastically tailored forward-swept wings. Structural and Multidisciplinary Optimization, 55(1), 105–119.
[5] Farsadi, T., & Hasbestan, J. J. (2019). Calculation of flutter and dynamic behavior of advanced composite swept wings with tapered cross-section in unsteady incompressible flow. Mechanics of Advanced Materials and Structures, 26(4), 314–332.
[6] Ibrahim R A, Castravete S C 2006 Flutter suppression of a plate-like wing via parametric excitation Journal of Reinforced Plastics and Composites 46(4).
[7] Guo S, Cheng W, Cui D 2005 Optimization of composite wing structures for maximum flutter speed 46th AIAA/ASME/ASCE/AHS/ASC Structures, Structural Dynamics and Materials Conference 2132.
[8] Fabbiane, N., Irisarri, F.-X., Dillinger, J.,& Lepage, A. (2022). Aeroelastic tailoring of a wind-tunnel model for passive alleviation of static and dynamic loads. CEAS Aeronautical Journal, 13(4), 967–977.
[9] Ritter, M., Meddaikar, M. Y., & Dillinger, J. (2017). Static and dynamic aeroelastic validation of a flexible forward-swept composite wing.
[10] Xue, R., Ye, Z., Ye, K.,& Wang, G. (2019). Composite material structure optimization design and aeroelastic analysis on forward swept wing. Proceedings of the Institution of Mechanical Engineers, Part G: Journal of Aerospace Engineering, 233(13), 4679–4695.
[11] Kawakami, K., & Kameyama, M. (2022). Optimum design of aft-swept composite wings for aeroelastic characteristics with structural damping. Saitekika Shinpojiumu Koen Ronbunshu, 2022.14.
[12] Farsadi, T., Ahmadi, M., Sahin, M., Haddad Khodaparast, H., Kayran, A., & Friswell, M. I. (2024). High aspect ratio composite wings: Geometrically nonlinear aeroelasticity, multi-disciplinary design optimization, manufacturing, and experimental testing. Aerospace.
[13] Kameyama, M., & Fukunaga, H. (2007). Optimum design of composite plate wings for aeroelastic characteristics using lamination parameters. Computers & structures, 85(3-4), 213-224.
[14] Mahran, M., Negmb, H., Maalawic, K., & El-Sabbaghd, A. (2015). Aero-elastic analysis of composite plate swept wings using the finite element method. Lisbon, Portugal.
[15] Aydogdu M 2008 Conditions for functionally graded plates to remain flat under in-plane loads by classical plate theory Journal of Composite Structures 82(1) 155–157.
[16] Reddy J N 2003 Mechanics of laminated composite plates and shells: theory and analysis.
[17] Landsberger B J 1983 Aeroelastic Properties of Straight and Forward Swept Graphite/Epoxy Wings.
[18] Jensen D W, Crawley E F, Dugundji J 1982 Vibration of cantilevered graphite/epoxy plates with bending-torsion coupling Journal of Reinforced Plastics and Composites 1(3) 254–269.
[19] Spielberg I N 1953 The Two-Dimensional Incompressible Aerodynamic Coefficients for Oscillatory Changes in Airfoil Camber Journal of the Aeronautical Sciences 20(6) 432–434